Fourth International Conference on Multiphase Flow, ICMF-2001
New Orleans, Louisiana, U.S.A, May 27 – June 1, 2001

3D volume-of-fluid simulation of a wobbling bubble in a gas-liquid system of low Morton number

W. Sabisch, M. Wörner*, G. Grötzbach, D.G. Cacuci

Forschungszentrum Karlsruhe GmbH, Institut für Reaktorsicherheit,
Postfach 3640, 76021 Karlsruhe, Germany

Abstract

A new computer code has been developed for the direct numerical simulation of certain aspects of three-dimensional bubble dynamics in a fluid. This code combines the Volume-of-Fluid method for tracking the gas-liquid interface with a new, piecewise linear, interface reconstruction algorithm called EPIRA. Results are presented for single gas bubbles rising in a plane vertical channel filled with a liquid. Four distinct combinations of Eötvös and Morton numbers, in the range $0.2 \leq Eö_B \leq 243$ and $2.5 \cdot 10^{-11} \leq M \leq 266$, are considered. Three of these combinations yield a spherical, ellipsoidal, and oblate ellipsoidal cap bubble, respectively, each rising steadily on a rectilinear path. For $Eö_B = 3.07$ and $M = 2.5 \cdot 10^{-10}$, a bubble with an irregular, oscillating wobbling shape rising on an irregular spiral path, is obtained. Even though the simulations were carried out with a gas-to-liquid density ratio of 0.5, all of the numerical results for bubble shape, wake, and path characteristics are in close agreement with the experimental results for gas-liquid systems characterized by the same values for $Eö_B$ and M, but having density ratios much smaller than 0.5.

1. Introduction

Although the fundamental physical understanding of the rise of gas bubbles in a continuous liquid is of significant practical importance for a variety of engineering applications, neither the interactions between bubbles rising in clusters nor the bubble-induced pseudo-turbulence (i.e., the generation of velocity fluctuations by bubbles and their wakes in an otherwise laminar flow) are fully understood yet. Modeling the bubble-induced pseudo-turbulence with the current generation of Computational Fluid Dynamics (CFD) codes requires detailed information about the full three-dimensional (3D) velocity field close to the bubble and in its wake. Such information, though, cannot be obtained experimentally yet, since even advanced experimental techniques, such as particle-image-velocimetry (PIV), can at best yield two-dimensional (2D) projections of the flow at any given instant in time (Brücker, 1999).

In the absence of detailed experimental information, the direct numerical simulation of the flow modeled by the Navier-Stokes equation can provide, in principle, a full 3D time-resolved velocity data field. The leading methods currently used for detailed numerical simulations of the hydrodynamics of single or multiple bubbles rising in a continuous liquid, where the gas-liquid interface is deformable, are the front-tracking method (Tryggvason et al., 1998), the level-set method (Sethian, 1999), and the Volume-of-Fluid (VOF) method (Kothe, 1998; Scardovelli and Zaleski, 1999) together with finite-difference discretization of the Navier-Stokes equation.

However, there are no reports in the open literature, to our knowledge, of applying the numerical methods mentioned above to 3D-problems involving Morton numbers M below $M \approx 10^{-10}$, where M is defined as

* Corresponding author. E-mail address: woerner@irs.fzk.de

$$M \equiv \frac{\left(\rho_l^* - \rho_g^*\right) g^* \mu_l^{*4}}{\rho_l^{*2} \sigma^{*3}}, \tag{1}$$

with ρ, μ, σ, g representing density, dynamic viscosity, surface tension, and gravity, respectively. The superscript (*) denotes dimensional quantities, while the subscripts *l* and *g* denote the liquid (continuous) and the gas (dispersed) phases, respectively. Most gas-liquid systems of practical relevance are characterized by very low Morton number; for example, $M \approx 10^{-11}$ for air bubbles in water, while the gas-liquid density ratio is about 1/1000.

To simulate systems characterized by very low Morton numbers, we have developed a new numerical method, which combines the Volume-of-Fluid interface tracking technique with the solution of the non-dimensional incompressible Navier-Stokes equations using a finite volume formulation on a staggered grid. For the interface reconstruction, we have developed a new piecewise linear algorithm (EPIRA), which reconstructs a linear three-dimensional interface (i.e. a plane) exactly. The purpose of this paper is to present our new numerical method together with illustrative 3D-results for single bubbles rising in a computationally periodic, plane vertical channel, for a gas-liquid density ratio of 0.5. In particular, we present results for the case $M = 2.5 \cdot 10^{-10}$, which show a shape-oscillating bubble in the "wobbling" regime, rising on an irregular spiral.

2. Governing equations

Since we use a finite volume method, we derive the governing equations by averaging the local equations over a volume *V*. With *f* denoting the liquid volumetric fraction within *V*, we define the mixture density and viscosity, respectively, as

$$\rho^* \equiv f \rho_l^* + (1-f) \rho_g^* \tag{2}$$

$$\mu^* \equiv f \mu_l^* + (1-f) \mu_g^* \tag{3}$$

and also define the center of mass velocity as

$$\vec{u}^* = \left(u^*, v^*, w^*\right)^{\mathrm{T}} \equiv \frac{f \rho_l^* \vec{u}_l^* + (1-f) \rho_g^* \vec{u}_g^*}{\rho^*}. \tag{4}$$

Both the liquid and gas are assumed to be incompressible Newtonian continua; furthermore, we assume that there is no slip between the phase velocities in interface mesh cells. Thus, the non-dimensional continuity and Navier-Stokes equation can be written as

$$\nabla \cdot \vec{u} = 0 \tag{5}$$

$$\frac{\partial \rho \vec{u}}{\partial t} + \nabla \cdot \left(\rho \vec{u} \otimes \vec{u}\right) = -\nabla p + \frac{1}{Re_{ref}} \nabla \cdot \left[\mu \left(\nabla \otimes \vec{u} + \left(\nabla \otimes \vec{u}\right)^{\mathrm{T}}\right)\right] - (1-f) \frac{E\ddot{o}_{ref}}{We_{ref}} \frac{\vec{g}^*}{g^*} + \frac{a_{int} \kappa \vec{n}}{We_{ref}}, \tag{6}$$

where $g^* = \left|\vec{g}^*\right| = 9.81 \mathrm{ms}^{-2}$, and where the various non-dimensional quantities are defined as follows:

$$\vec{x} = \begin{pmatrix} x \\ y \\ z \end{pmatrix} = \frac{\vec{x}^*}{L_{ref}^*}, \; \vec{u} = \frac{\vec{u}^*}{U_{ref}^*}, \; t = \frac{t^* U_{ref}^*}{L_{ref}^*}, \; \rho = \frac{\rho^*}{\rho_l^*}, \; \mu = \frac{\mu^*}{\mu_l^*}, \; p = \frac{p^* - \rho_l^* \vec{g}^* \cdot \vec{x}^*}{\rho_l^* U_{ref}^{*2}}. \tag{7}$$

The derivations leading to Eqs. (5) and (6) are detailed in the paper by Wörner et al. (2001, this conference). The dimensionless groups in Eq. (6) are the reference Reynolds, Eötvös, and Weber numbers, respectively, defined as

$$Re_{ref} \equiv \rho_l^* L_{ref}^* U_{ref}^* / \mu_l^* , \quad E\ddot{o}_{ref} \equiv \left(\rho_l^* - \rho_g^*\right) g^* L_{ref}^{*\,2} / \sigma^* , \quad We_{ref} \equiv \rho_l^* L_{ref}^* U_{ref}^{*\,2} / \sigma^* . \tag{8}$$

By replacing, in Eq. (8), L^*_{ref} by the bubble equivalent diameter d^*_e and, respectively, U^*_{ref} by the terminal rise velocity U_T^* of the bubble, we obtain the bubble Reynolds (Re_B), bubble Eötvös ($E\ddot{o}_B$), and bubble Weber number (We_B). The Morton number is related to the Reynolds, Eötvös and Weber numbers by means of the relation

$$M = E\ddot{o}_{ref} We_{ref}^2 / Re_{ref}^4 = E\ddot{o}_B We_B^2 / Re_B^4 . \tag{9}$$

The last term on the right-side of Eq. (6) is due to surface tension; in that term, a_{int}, κ, and $\vec{n}$ denote the (non-dimensional) interfacial area concentration, mean interface curvature and mean unit normal vector to the interface within the averaging volume V.

The above set of equations is completed by the transport equation for the liquid volumetric fraction

$$\frac{\partial f}{\partial t} + \nabla \cdot \left(f \vec{u}\right) = 0 \tag{10}$$

which can be derived from the continuity equation for the liquid phase.

3. Numerical Method

3.1. EPIRA algorithm for interface reconstruction

We have developed a new algorithm, called EPIRA, which yields a linearly-accurate interface reconstruction on a 3D structured orthogonal non-equidistant fixed grid. The acronym EPIRA stands for "Exact Plane Interface Reconstruction Algorithm". The algorithm belongs to the class of PLIC (Piecewise Linear Interface Calculation) methods. EPIRA reconstructs a plane 3D-interface exactly, regardless of its orientation; in this sense, EPIRA is second-order accurate. In this sub-section, we provide a short description of the EPIRA reconstruction step. Additional details can be found in the works of Sabisch et al. (1999) and Sabisch (2000).

In EPIRA, we assume a functional interface of zero thickness, which can locally be described by a single valued height function $\xi = h(\zeta, \eta)$, where (ζ, η, ξ) define a local Cartesian coordinate-system. Expanding $h(\zeta, \eta)$ in a Taylor-series around the point $0 \equiv (\zeta_0, \eta_0)$ yields

$$h(\zeta,\eta) = h_0 + (\zeta - \zeta_0)\left.\frac{\partial h(\zeta,\eta)}{\partial \zeta}\right|_0 + (\eta - \eta_0)\left.\frac{\partial h(\zeta,\eta)}{\partial \eta}\right|_0 + (\zeta - \zeta_0)(\eta - \eta_0)\left.\frac{\partial^2 h(\zeta,\eta)}{\partial \zeta \partial \eta}\right|_0 + \ldots . \tag{11}$$

We approximate locally the interface by a plane by retaining only the first three terms on the right-side of Eq. (11), namely:

$$h(\zeta,\eta) \cong h_0 + \alpha(\zeta - \zeta_0) + \beta(\eta - \eta_0). \tag{12}$$

This approximation is reasonable if (ζ, η) is close to (ζ_0, η_0) or if the interface curvature is small.

To reconstruct the interface orientation and position, we need to determine a vector $\vec{n} = (n_\zeta, n_\eta, n_\xi)^T$ normal to the interface, and a point (b_ζ, b_η, b_ξ) within the interface. For this purpose, we consider a rectangular cell (i,j,k) with a liquid volumetric fraction satisfying $0 < f_{i,j,k} < 1$. For each of the six faces of the interface-cell (i,j,k), we check to see if the respective face happens to be a gas/liquid (g/l)-interface-face. Thus, face E(ast) located at $x_{i+1/2}$ is a g/l-interface-face if $0 < f_{i+1,j,k} < 1$; the faces W(est) at $x_{i-1/2}$, N(orth) at $z_{k+1/2}$, S(outh) at $z_{k-1/2}$, F(ront) at $y_{j-1/2}$ and B(ack) at $y_{j+1/2}$ are checked similarly.

Next, we determine a tangential vector for each g/l-interface-face, as illustrated in Fig. 1 for face E, where, without loss of generality, we assume that the local co-ordinate system (ζ, η, ξ) coincides with the global co-ordinate system (x,y,z). If the plane $h(\zeta, \eta)$ does not cut the upper or lower faces of the adjacent cells (i,j,k) and $(i+1,j,k)$, then $N_{i,j,k}$, $S_{i,j,k}$, $N_{i+1,j,k}$ and $S_{i+1,j,k}$ are not g/l-interface-faces.

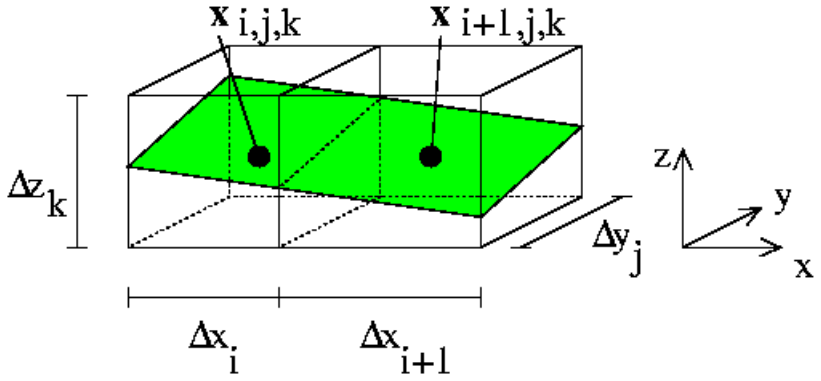

Fig. 1:
Cells (i,j,k) and $(i+1,j,k)$ with plane $h(x,y)$ representing the interface. The fluid is below $h(x,y)$.

It hence follows that

$$f_{i,j,k} = \frac{1}{\Delta x_i \Delta y_j \Delta z_k} \int_0^{\Delta x_i} \int_0^{\Delta y_j} h(x,y)\,dy\,dx, \quad f_{i+1,j,k} = \frac{1}{\Delta x_{i+1} \Delta y_j \Delta z_k} \int_{\Delta x_i}^{\Delta x_i + \Delta x_{i+1}} \int_0^{\Delta y_j} h(x,y)\,dy\,dx\,. \tag{13}$$

Inserting Eq. (12) in Eq. (13), performing the integrations, and subtracting $f_{i,j,k}$ from $f_{i+1,j,k}$ yields

$$\alpha_E = \alpha_{i+1/2,j,k} = \frac{2\Delta z_k}{\Delta x_i + \Delta x_{i+1}} \cdot \left(f_{i+1,j,k} - f_{i,j,k} \right). \tag{14}$$

Since α_E represents the slope of the interface in the x-direction, it follows that the unit tangential vector $\vec{t}_E$ is obtained as

$$\vec{t}_E = \frac{1}{\sqrt{1+\alpha_E^2}} \begin{pmatrix} 1 \\ 0 \\ \alpha_E \end{pmatrix}. \tag{15}$$

Note that this tangential vector is exact for any planar interface, if the lower and upper integration limits in Eq. (13) are correct. As mentioned above, this requires that $N_{i,j,k}$, $S_{i,j,k}$, $N_{i+1,j,k}$ and $S_{i+1,j,k}$ are not g/l-interface-faces. Otherwise, the integration limits must be adjusted to account for the intersections of the g/l-interface with the lower upper cell faces, respectively. Such adjustments would require the consideration of several distinct situations and would be computationally ineffective.

Figure 2a depicts a case where, even though the face $N_{i,j,k}$ is a g/l-interface-face, α_E can still be determined exactly. For this purpose, we extend the domain for computing α_E by considering *a pair* of double-cells, $(i,j,k)+(i,j,k+1)$ and $(i+1,j,k)+(i+1,j,k+1)$, respectively (see Fig. 2b). For each double-cell, Eq. (13) can be used again to obtain α_E and $\vec{t}_E$ exactly, by replacing Δz_k with $\Delta z_k+\Delta z_{k+1}$ on the right-side of Eq. (13), and $f_{i,j,k}+f_{i,j,k+1}$ (instead of $f_{i,j,k}$) and $f_{i+1,j,k}+f_{i+1,j,k+1}$ (instead of $f_{i+1,j,k}$) on the respective left-sides. A similar procedure is used when $S_{i,j,k}$ or $S_{i+1,j,k}$ are g/l-interface-faces.

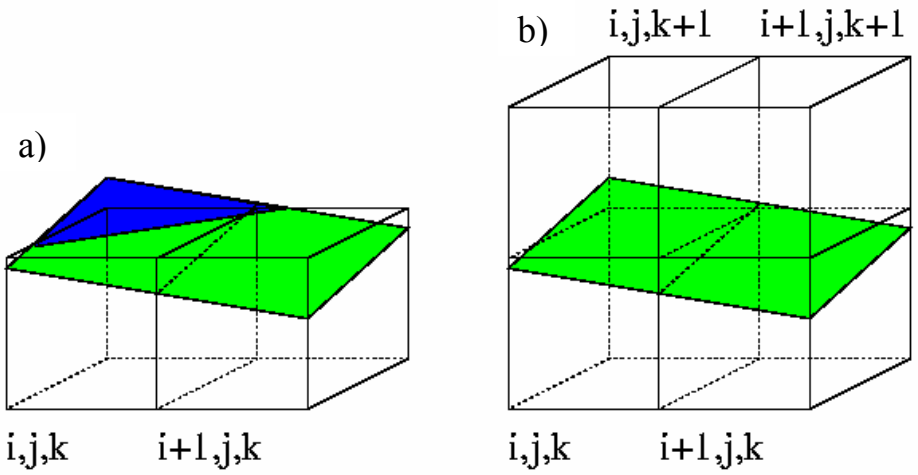

Fig. 2:
a): Example where $N_{i,j,k}$ is a g/l-interface-face.
b): An extension of the left and right volumes is performed to obtain the slope α_E exactly.

When $N_{i,j,k+1}$, $N_{i+1,j,k+1}$, $S_{i,j,k-1}$ or $S_{i+1,j,k-1}$ are g/l-interface-faces, one upper and/or lower extension is still insufficient to obtain α_E exactly. Since we do not wish to lose the locality of the reconstruction, though, we perform at most one extension above and/or one below the basic pair of cells. If this is not sufficient to determine a value for α_E, then we guess a value for it by setting the slope β in Eq. (12) to zero and thereby simplifying the 3D-problem to a 2D one. By considering four possible different cases for the resulting 2D-problem (see Figure 3), the slope α_E is determined analytically via a case check diagram according to the 2D FLAIR algorithm of Ashgriz and Poo (1991), which was extended by us to non-equidistant grids. Using this approximate (2D-) value for α_E in Eq. (15) yields an approximate value for $\vec{t}_E$.

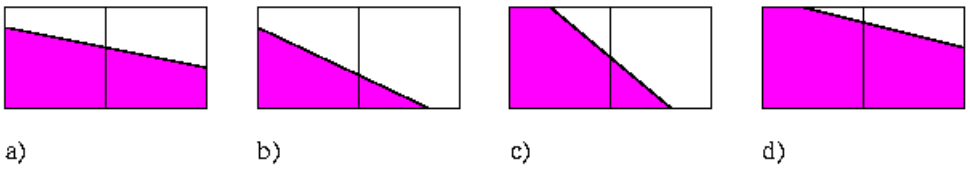

Fig. 3: Four cases of 2D FLAIR algorithm.

Thus, a unit tangential vector is computed using the above procedure at each of the (minimum three and maximum six) g/l-interface-faces of an interface mesh cell. The unit tangential vector thus computed is flagged as *exact,* if the slope is determined via Eq. (14), or as *inexact*, if it is computed using the extended 2D FLAIR algorithm. For computational reasons, we set the tangential vector to the null vector when a face is not a g/l-interface-face.

From the tangential vectors at the different faces of cell (*i,j,k*), we compute a cell-centered unit normal vector, $\vec{n}_{i,j,k}$, for each interface cell. We demonstrate this computation for cell (*i,j,k*), as illustrated in Fig. 1, where $\vec{t}_N$ and $\vec{t}_S$ are zero, whereas $\vec{t}_E$, $\vec{t}_W$, $\vec{t}_F$ and $\vec{t}_B$ are not. For each co-ordinate direction, we determine a *representative* tangential vector as follows: if $\vec{t}_E$ and $\vec{t}_W$ are marked with the same flag (i.e., both exact or both inexact), then $\vec{t}_{EW}$ is obtained by taking their average, namely $\vec{t}_{EW} = \left(\vec{t}_E + \vec{t}_W\right) \Big/ \left|\vec{t}_E + \vec{t}_W\right|$. Otherwise, either $\vec{t}_E$ or $\vec{t}_W$ can be selected as representative, although the exact one is to be preferred. We flag $\vec{t}_{EW}$ as *exact* if $\vec{t}_E$, $\vec{t}_W$, or both are exact. The other representative unit tangential vectors, $\vec{t}_{NS}$ and $\vec{t}_{FB}$, are determined similarly. Using these three representative unit tangential vectors, the (minimum one and maximum three) *preliminary* unit normal vectors are computed as shown below:

$$\vec{n}_1 = \frac{\vec{t}_{EW} \times \vec{t}_{NS}}{\left|\vec{t}_{EW} \times \vec{t}_{NS}\right|}, \quad \vec{n}_2 = \frac{\vec{t}_{NS} \times \vec{t}_{FB}}{\left|\vec{t}_{NS} \times \vec{t}_{FB}\right|}, \quad \vec{n}_3 = \frac{\vec{t}_{FB} \times \vec{t}_{EW}}{\left|\vec{t}_{FB} \times \vec{t}_{EW}\right|}. \tag{16}$$

If necessary, each of these preliminary normal vectors is re-orientated to point inside the fluid. By averaging these preliminary normal vectors using the same steps as used for obtaining the representative tangential unit vectors, we obtain, ultimately, the *representative* cell-centered unit normal vector. For the situation illustrated in Fig. 1, the vector $\vec{t}_{NS}$ is zero, which implies that only the normal vector $\vec{n}_3$ is non-zero; no averaging is required.

By shifting iteratively the interface-representing plane until the correct liquid volumetric fraction within the mesh cell is recovered, the interface reconstruction is ultimately completed by determining the point (b_ζ, b_η, b_ξ).

The fluxes of the liquid phase across the faces of the cells are computed in the advection step using the *naive unsplit method*. The liquid fluxes in the three co-ordinate directions are computed simultaneously, based on only one reconstruction step for each time step. A cuboid of influence is defined close to each face; the cuboid's base is the respective cell-face and its depth is the respective face-centered velocity multiplied by the time step width.

When the flow is oblique to the cell faces, the three cuboids of influence overlap in the naive unsplit method, and liquid volume may be advected twice. In such a case, as well as in cases of low bubble resolution and/or high interface curvature, it can happen that, after the advection step, there remain interface-cells containing a very small fraction of fluid, ε, or gas, 1-ε, and only two g/l-interface-faces. Such a configuration is not meaningful for EPIRA, so we redistribute the fluid or gas to neighboring interface-cells. The value of ε is related to the residuum of the divergence of the velocity field, which is set to 10^{-5} in our simulations.

3.2. Solution strategy

The EPIRA algorithm has been implemented in our in-house code TURBIT-VOF, which solves the conservation equation for f together with the non-dimensional continuity and the Navier-Stokes equations shown in Eqs. (5) and (6). TURBIT-VOF is designed to simulate flows in plane channels. It employs a staggered grid, uniform in the x- and y-directions (parallel to the walls), but possibly non-uniform in z-direction (normal to the walls). The solution strategy is based on a projection method. The predictor step includes the convection, friction, and buoyancy terms, namely

$$\begin{aligned}\frac{\partial(\rho\vec{u})^{\sim}}{\partial t} &= -\nabla\cdot(\rho\vec{u}\otimes\vec{u}) + \frac{1}{Re_{ref}}\nabla\cdot\left[\mu\left(\nabla\otimes\vec{u}+(\nabla\otimes\vec{u})^{T}\right)\right] - (1-f)\frac{E\ddot{o}_{ref}}{We_{ref}}\frac{\vec{g}^{*}}{|\vec{g}^{*}|} \\ &= -\vec{C}+\vec{F}-\vec{B} = \vec{L}(\rho,\mu,\vec{u},f).\end{aligned} \tag{17}$$

This predictor step is performed by an explicit third order Runge-Kutta scheme as sketched below:

$$\begin{aligned}\rho^{(1)}\vec{u}^{(1)} &= \rho^{n}\vec{u}^{n} + \Delta t\, L\left(\rho^{n},\mu^{n},\vec{u}^{n},f^{n}\right) \\ \rho^{(2)}\vec{u}^{(2)} &= \frac{3}{4}\rho^{n}\vec{u}^{n} + \frac{1}{4}\rho^{(1)}\vec{u}^{(1)} + \frac{1}{4}\Delta t\, L\left(\rho^{(1)},\mu^{(1)},\vec{u}^{(1)},f^{(1)}\right) \\ \rho^{\sim}\vec{u}^{\sim} &= \frac{1}{3}\rho^{n}\vec{u}^{n} + \frac{2}{3}\rho^{(2)}\vec{u}^{(2)} + \frac{2}{3}\Delta t\, L\left(\rho^{(2)},\mu^{(2)},\vec{u}^{(2)},f^{(2)}\right).\end{aligned} \tag{18}$$

For the intermediate time levels, we set

$$f^{(1)} = f^{(2)} = f^{n+1}, \quad \rho^{(1)} = \rho^{(2)} = \rho^{\sim} = \rho^{n+1}, \quad \mu^{(1)} = \mu^{(2)} = \mu^{n+1}. \tag{19}$$

Treating the pressure term and surface tension term implicitly, the corrector step is

$$\frac{\rho^{n+1}\vec{u}^{n+1} - \rho^{\sim}\vec{u}^{\sim}}{\Delta t} = -\nabla p^{n+1} + \vec{S}^{n+1}. \tag{20}$$

Applying the divergence operator to Eq. (20) and introducing the continuity equation $\nabla\cdot\vec{u}_{m}^{n+1} = 0$ yields the Poisson equation

$$\nabla\cdot\left(\frac{\Delta t}{\rho_{m}^{n+1}}\nabla p^{n+1}\right) = \nabla\cdot\vec{u}_{m}^{\sim} + \nabla\cdot\left(\frac{\Delta t}{\rho_{m}^{n+1}}\vec{S}^{n+1}\right). \tag{21}$$

A Conjugate Gradient solver (Schönauer et al., 1997) is used to solve the above Poisson equation. Alternatively, the buoyancy term can be included in the corrector step rather than in the predictor step; we found that this procedure is numerically advantageous for free surface flows.

3.3. Spatial discretization on a staggered grid

A second order central difference scheme is used to discretize the diffusive and non-linear convective terms in the Navier-Stokes equation. For treating the convective terms, we are currently developing a high resolution WENO (Weighted Essentially Non Oscillatory) discretization scheme

with one-dimensional reconstruction along each co-ordinate direction. WENO shock capturing schemes were originally developed for compressible single phase flows. The WENO scheme intended for TURBIT-VOF is envisaged to minimize the numerical smearing when computing the convective terms, for low gas/liquid density ratios, within the three sub-integration steps of the Runge-Kutta time integration procedure. For the gas/liquid density ratio of 0.5 considered in the present paper, we found that the results obtained with the central difference scheme agree well with those obtained with the WENO scheme presently implemented in TURBIT-VOF.

Within the staggered grid used in TURBIT-VOF, the density, viscosity and the liquid volumetric fraction $f_{i,j,k}$ are cell-centered, while the control volumes for the three components of the Navier-Stokes equation are shifted by half a mesh-width to obtain the velocity components as $u_{i+1/2,j,k}$, $v_{i,j+1/2,k}$, $w_{i,j,k+1/2}$. For the spatial discretization of the various terms in the Navier-Stokes equation, though, we need velocities at centered positions, and the density and viscosity at shifted positions, respectively. In the current version of TURBIT-VOF, which does not consider mass transfer, the velocities at centered positions are obtained from a linear interpolation, which is justified since the velocity is continuous across the interface (in the absence of mass transfer). The density and viscosity, however, are discontinuous across the interfaces, so that a linear interpolation may introduce large errors. For this reason, we compute these quantities by a different method as follows: taking into account the actual interface location in cell (i,j,k) and cell $(i+1,j,k)$, we compute the liquid volumes within the half-cells $[x_{i,j,k},\ x_{i+1/2,j,k}] \times [y_{i,j-1/2,k},\ y_{i,j+1/2,k}] \times [z_{i,j,k-1/2},\ z_{i,j,k+1/2}]$ and $[x_{i+1/2,j,k},\ x_{i+1,j,k}] \times [y_{i,j-1/2,k},\ y_{i,j+1/2,k}] \times [z_{i,j,k-1/2},\ z_{i,j,k+1/2}]$, respectively. We then add both liquid volumes together and divide the resulting sum by the total volume of both half-cells to obtain $f_{i+1/2,j,k}$. Having thus obtained $f_{i+1/2,j,k}$ allows us to compute $\rho_{i+1/2,j,k}$. The quantity $f_{i+1/2,j+1/2,k}$ is computed similarly, by considering four quarter-cells.

3.4. Discretization of the surface tension term

In this subsection, we illustrate the dicretization procedure for the first component of the source term due to surface tension in the Navier-Stokes equation; the other components are obtained similarly. In principle, we must compute source terms of the form

$$S_{i+1/2,j,k} = \frac{1}{We_{ref}} a_{int;i+1/2,j,k} \kappa_{i+1/2,j,k} \vec{n}_{i+1/2,j,k} \,. \tag{22}$$

The EPIRA reconstruction algorithm yields the interface unit normal vector at cell centers (i,j,k). The staggered interface unit normal vector is obtained from the interpolation

$$\vec{n}_{i+1/2,j,k} = \frac{\vec{n}_{i,j,k} + \vec{n}_{i+1,j,k}}{\left| \vec{n}_{i,j,k} + \vec{n}_{i+1,j,k} \right|} \,. \tag{23}$$

Note that $\vec{n}_{i,j,k}$ is initialized as the null vector in any cell which is not an interface mesh cell. Next, we follow Brackbill et al. (1992) to compute the curvature from the gradient of the unit normal vector, $\kappa = -\nabla \cdot \vec{n}$. For the first component of the Navier-Stokes equation, this procedure gives

$$\kappa_{i+1/2,j,k} = -\left(\frac{n_{x;i+1,j,k} - n_{x;i,j,k}}{\Delta x} + \frac{n_{y;i+1/2,j+1/2,k} - n_{y;i+1/2,j-1/2,k}}{\Delta y} + \frac{n_{z;i+1/2,j,k+1/2} - n_{z;i+1/2,j,k-1/2}}{\Delta z_k} \right). \tag{24}$$

The staggered values of the unit normal vector in Eq. (24) are obtained by interpolation as:

$$\vec{n}_{i+1/2,j\pm1/2,k} = \frac{\vec{n}_{i,j,k} + \vec{n}_{i,j\pm1,k} + \vec{n}_{i+1,j,k} + \vec{n}_{i+1,j\pm1,k}}{\left| \vec{n}_{i,j,k} + \vec{n}_{i,j\pm1,k} + \vec{n}_{i+1,j,k} + \vec{n}_{i+1,j\pm1,k} \right|}, \quad \vec{n}_{i+1/2,j,k\pm1/2} = \frac{\vec{n}_{i,j,k} + \vec{n}_{i,j,k\pm1} + \vec{n}_{i+1,j,k} + \vec{n}_{i+1,j,k\pm1}}{\left| \vec{n}_{i,j,k} + \vec{n}_{i,j,k\pm1} + \vec{n}_{i+1,j,k} + \vec{n}_{i+1,j,k\pm1} \right|} \,. \tag{25}$$

The interfacial area concentration $a_{int;i+1/2,j,k}$ is computed by adding the areas of the interfaces in the two half-cells $[x_{i,j,k},\ x_{i+1/2,j,k}] \times [y_{i,j-1/2,k},\ y_{i,j+1/2,k}] \times [z_{i,j,k-1/2},\ z_{i,j,k+1/2}]$ and $[x_{i+1/2,j,k},\ x_{i+1,j,k}] \times [y_{i,j-1/2,k},\ y_{i,j+1/2,k}] \times [z_{i,j,k-1/2},\ z_{i,j,k+1/2}]$, and dividing the result by the total volume of both half-cells.

3.5. *Code verification*

Several prototypical interfacial problems have been considered, as detailed by Sabisch (2000), to verify TURBIT-VOF. E.g., the computational accuracy of the surface tension model has been verified by simulating capillary waves. In this benchmark problem, the surface tension acts as the sole driving force on an initially sinusoidal interface at rest. The temporal development of the oscillation damped by viscosity has been computed by TURBIT-VOF, and it agrees well with the respective analytical solution. Furthermore, the calculation of the buoyancy force has been verified by simulating both gravity waves and the Rayleigh-Taylor instability, starting with a sinusoidal interface initially at rest. Also in the case of gravity waves, the computed oscillation of the interface damped by viscosity agrees well with the respective analytical solution. Both 2D and 3D configurations have been considered for computing the respective Rayleigh-Taylor instabilities. The computed velocities of the rising "bubble" and the falling "finger" are in excellent agreement with values from literature. As detailed by Sabisch (2000), very good agreements between numerical and analytical solutions have also been obtained for other interfacial problems used to verify the new numerical procedures implemented in TURBIT-VOF.

4. Simulation parameters

4.1. *Physical parameters*

The relevant physical quantities for a bubble rising with its terminal velocity through an *infinite* liquid are included in the following equation (Grace, 1973)

$$F^*\left(g^*,\rho_l^*,\mu_l^*,\sigma^*,\rho_g^*,\mu_g^*,d_e^*,U_T^*\right)=0\,. \tag{26}$$

The above equation may be rewritten in terms of five independent dimensionless groups as

$$F\left(Re_B,Eo_B,M,\Gamma_\rho,\Gamma_\mu\right)=0, \tag{27}$$

where $\Gamma_\rho=\rho_g^*/\rho_l^*$ and $\Gamma_\mu=\mu_g^*/\mu_l^*$ are the density and viscosity ratios, respectively. In the simulations reported in this paper, $Eö_B$, M, Γ_ρ and Γ_μ have been held fixed, and the simulations were performed for four different combinations of ($Eö_B$, M) as shown in Table 1. According to the "Re_B versus $Eö_B$" diagram of Clift et al. (1978) we expect for cases ❶, ❷, and ❹ to obtain a bubble with a steady shape (ellipsoidal, oblate spherical cap, and spherical, respectively), rising steadily along a rectilinear path. The bubble for case ❸ is expected to be in the "wobbling" regime.

For all bubble simulations presented in Table 1, the density ratio is Γ_ρ=0.5 and the viscosity ratio is Γ_μ=1. Setting h_{min}=min$_k$(Δx, Δy, Δz_k), the convective, viscous, and capillary time step criterion are

$$\Delta t_{CFL}\le\frac{h_{min}}{\max\limits_{i,j,k}\left|\vec{u}^n\right|},\quad \Delta t_\mu\le\frac{h_{\min}^2 Re_{ref}}{6}\cdot\min\left(1,\frac{\Gamma_\rho}{\Gamma_\mu}\right),\quad \Delta t_\sigma\le\sqrt{\frac{h_{min}^3}{4\pi}We_{ref}\left(1+\Gamma_\rho\right)}\,. \tag{28}$$

Table 1: Physical and numerical parameters for TURBIT-VOF simulations

Case	$Eö_B$	M	Re_{ref}	We_{ref}	L_x	L_y	L_z	N_x	N_y	N_z	d_e
❶ (a)	3.07	$3.1\cdot10^{-6}$	100	2.5	2	1	1	128	64	64	0.25
❶ (b)	3.07	$3.1\cdot10^{-6}$	100	2.5	1	1	1	64	64	64	0.25
❶ (c)	3.07	$3.1\cdot10^{-6}$	200	5	½	½	1	64	64	128	0.125
❶ (d)	3.07	$3.1\cdot10^{-6}$	100	2.5	1	1	1	128	128	128	0.25
❷	243	266	13.2	45.8	1	1	1	64	64	64	0.25
❸	3.07	$2.5\cdot10^{-10}$	999.6	2.5	1	1	1	64	64	64	0.25
❹	0.2	$2.5\cdot10^{-11}$	1050	2.5	1	1	1	64	64	64	0.25

The formula for Δt_μ in the inequalities above indicates that low values of Γ_ρ lead to stiff problems, in the sense that the diffusive time scales of the gas and liquid phases become significantly distinct from each other. For cases ❶ (a-c), for example, Δt_{CFL}, Δt_μ, and Δt_σ are of same order of magnitude ($\Delta t_{max} \approx 0.002$) when $\Gamma_\rho = 0.5$. For a smaller value of Γ_ρ, the viscous time step criterion will become the most stringent among all. Due to the discontinuity at the interface, very low density ratios also produce numerical difficulties when computing the convective terms, and would therefore likely need a much higher mesh-cell resolution of the bubble than is necessary for $\Gamma_\rho = 0.5$.

4.2. Grid parameters, boundary conditions, and initial conditions

Numerical simulations have also been performed for a bubble rising between two parallel plane vertical walls, using a non-dimensional wall distance $L_z = L^*_z / L^*_{ref} = 1$ and no slip boundary conditions at z=0 and z=1. In the vertical (x) and span-wise (y) directions, we have used periodic boundary conditions, with periodicity lengths L_x and L_y, respectively. The orientation is such that the gravity vector points in the negative x-direction. Thus, the results to be presented in section 5 below will refer to the rise of a *regular array of bubbles*, as opposed to the rise of a single bubble.

The simulations were performed on uniform grids consisting of $N_x \cdot N_y \cdot N_z$ cubical mesh cells. As Table 1 shows, most of the simulations were carried out for a cubical computational domain discretized by 64x64x64 mesh cells, where $L^*_{ref} = 4\text{m}$ and $U^*_{ref} = 1\text{ms}^{-1}$. This discretization allows a 16-mesh-cells resolution of the non-dimensional bubble equivalent diameter $d_e = 0.25$, and corresponds to a total gas content of about 0.8%.

The periodic boundary conditions used in the numerical simulations mentioned in Table 1 allow only a qualitative comparison with experiments for single bubbles rising in an infinite liquid. Also, since we considered a *finite* channel, the function F^* in Eq. (26) would need to include additional dimensional quantities, since, for bubbles rising in a channel or a pipe, U^*_T is also influenced by the ratio of the bubble equivalent diameter to the channel hydraulic diameter. In our simulations, this ratio is $\lambda = 0.5\, d_e L_z$, and has typically the value 1/8. According to Clift et al. (1987, formula 9-35), the terminal-rise velocity in this case is reduced by less than 3% due to wall effects, as compared to the terminal-rise velocity of a freely rising bubble. Therefore, we can neglect the wall effects for the cases presented in Table 1.

For all of the simulations of case ❶, the fluid and gas were initially at rest. To save CPU time, the simulations for cases ❷, ❸, and ❹ were not initialized from stagnant conditions but from the final flow state of run ❶ (b). The computations were performed on a single processor of a vector-parallel SNI VPP 300. Due to its transient nature, case ❸ is the most expensive computationally; the total CPU time required was about 100 hours.

5. Results

In the following two subsections, we assess the influence of the density ratio of 0.5 used in our simulations by comparing the numerical results for cases ❶ and ❷ with experimental data for gas-liquid systems in which the Morton and Eötvös numbers were the same as used in the numerical simulations, but where the density ratios were of the order of 10^{-3}. In subsection 5.3, we discuss results for case ❸, which simulates a wobbling bubble. For case ❹, the Morton number corresponds to that of an air-water system. Additional details for this case are given by Sabisch (2000), who obtained a steady, almost spherical, bubble that rises rectilinearly.

5.1. Ellipsoidal bubble ($E\ddot{o}_B = 3.07$, $M = 3.1 \cdot 10^{-6}$)

Based on experiments for fifty-four dispersed-continuous phase systems, Wellek et al. (1966) derived empirical relations for the eccentricity E of non-oscillating bubbles and drops, over a wide range of particle Reynolds numbers. For $E\ddot{o}_B < 40$ and $M \leq 10^{-6}$, they obtained the relation

$$E = \left(1 + 0.163 E\ddot{o}_B^{0.757}\right)^{-1}. \tag{29}$$

In our simulation, we have obtained (after a transient from the initial spherical shape) an ellipsoidal bubble rising steadily on a rectilinear path, with an confined recirculation zone at its rear. The bubble's eccentricity was obtained as $E = 0.71$ for case ❶ (a); this value agrees well with the value $E = 0.72$ obtained from Eq. (29) for $E\ddot{o}_B = 3.07$. Also, we computed the bubble Reynolds number as $Re_B = 61.5$, and this value lies well within the range of 50 to 70, as observed in experiments (Clift et al., 1978). From these results, we concluded that the density and viscosity ratios play only minor roles in this case.

Cases ❶ (b) and (c) depict the influence of the size of the computational domain, since we use the same bubble resolution as in case ❶ (a). The ratio L_x / d_e is a measure for the influence of the periodic boundary conditions on the vertical distance between consecutive bubbles. The lower the ratio L_x / d_e, the stronger the influence of the periodic boundary conditions. Table 2 shows that reducing the ratio $L_x / d_e = 8$ used in case (a) to $L_x / d_e = 4$ in cases (b) and (c) leads to an increase of Re_B of about 10%. This increase of the bubble rise velocity is to be expected because the bubble comes closer to the "leading" bubble and thus experiences a smaller drag. By using the same computational domain but halving the mesh width of case ❶ (b), we study in case ❶ (d) the influence of the grid size and bubble resolution $d_e / \Delta x$. As the results presented in Table 2 show, the grid refinement has only a very small effect on Re_B and We_B.

Table 2: Re_B and We_B for the different domain sizes and grids of case ❶

	case ❶ (a)	case ❶ (b)	case ❶ (c)	case ❶ (d)
L_x / d_e	8	4	4	4
$d_e / \Delta x$	16	16	16	32
Re_B	61.5	67.5	67.0	66.0
We_B	1.54	1.69	1.68	1.65

5.2. Oblate ellipsoidal cap bubble ($E\ddot{o}_B = 243$, $M = 266$)

The Eötvös and Morton numbers of case ❷ correspond to those found in an experiment by Bhaga and Weber (1981), as they investigated an air bubble rising in aqueous sugar solution with $\Gamma_\rho \approx 1/1000$. Fig. 4 shows the stationary bubble shape in experiment and simulation, respectively. The oblate ellipsoidal cap bubble shows the typical impression at its rear. In the experiment, the bubble is slightly more oblate than in the simulation. The reason is presumably due to the periodic boundary conditions we have used in the simulation. The important effect of the periodicity length in the direction in which the bubble rises was already discussed in the foregoing. For case ❷, we have not yet investigated the influence of L_x / d_e. Therefore, we cannot preclude that the difference in shape in Fig. 4 may partly be due to the difference in density and viscosity ratios between the experiment and our simulation.

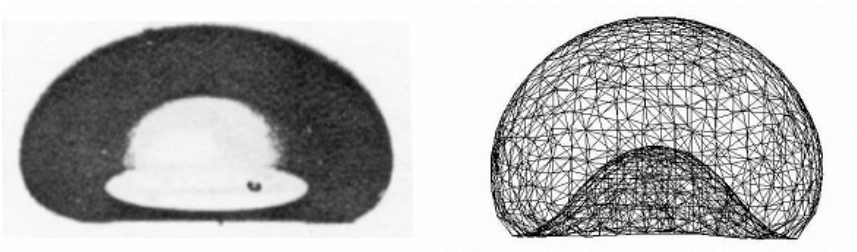

Fig. 4:
Steady bubble shape for $E\ddot{o}_B = 243$, $M = 266$ in experiment (Bhaga and Weber, 1981) (left) and simulation (right).

5.3. *Wobbling bubble* ($Eö_B$ = 3.07, $M = 2.5 \cdot 10^{-10}$)

The simulation for case ❷ has been initialized from the final state of simulation ❶ (b), having the same Eötvös number $Eö_B$ = 3.07 but a larger Morton number ($M = 3.1 \cdot 10^{-6}$). The Morton number has been stepwise decreased by increasing Re_{ref} stepwise, typically by one hundred, from 100 to 1050. A hundred time steps were computed for each intermediate Re_{ref}. About 6000 additional time steps were computed after the Morton number reached its end value of $M=2.5 \cdot 10^{-10}$. Altogether, this procedure has simulated a vertical travel distance of about 16 times d_e or, equivalently, about four times the height of the computational domain. The bubble Reynolds number reached in this simulation was about 1000.

The trajectory of the bubble's center of mass is depicted in Fig. 5, which shows that the initially rectilinear path becomes unstable as the bubble rises. Initially, the bubble performs a lateral motion in a *x*-*z*-plane, which already starts in the initial transient, when M is decreased to $7.5 \cdot 10^{-9}$. Associated with the path instability, we observe small asymmetries in the bubble shape. Once the bubble has risen to about the height of the computational domain, when $M \approx 3.7 \cdot 10^{-10}$ is reached, the lateral motion is also observed in the *x*-*y*-plane. In the *y*-*z*-plane-view presented in Fig. 5 (d), a spiral motion is observed in accordance with the irregular helical path followed by the bubble. Overall, this transition occurs very fast, presumably because of the periodic boundary conditions, which cause the bubble to interact with its own wake, thereby strongly amplifying small disturbances.

Fig. 6 shows one instantaneous bubble shape together with velocity vectors and vorticity contour lines in the plane z=0.5. The respective visualization displays the structure of the wake, which is open and displays small vortices associated with the bubble-induced turbulence. Although it is well known that bubbles with $Re_B=O(1000)$ may undergo irregular shape oscillations and rise on more or less regular zigzag, rocking or spiral paths (Clift et al., 1998; Fan and Tsuchiya, 1990), it is very difficult to perform quantitative or even qualitative comparisons of the present results with experimental investigations, such as those of Brücker (1999) or Stewart (1995), for example. This is due not only to the channel geometry and periodic boundary conditions used in our simulations, but also to the fundamental difficulty of describing the complex shape, motion and wake characteristics of wobbling bubbles. Furthermore, the dynamics of such bubbles is strongly influenced by the presence of surface-active contaminants, an effect that is not taken into account in our simulations.

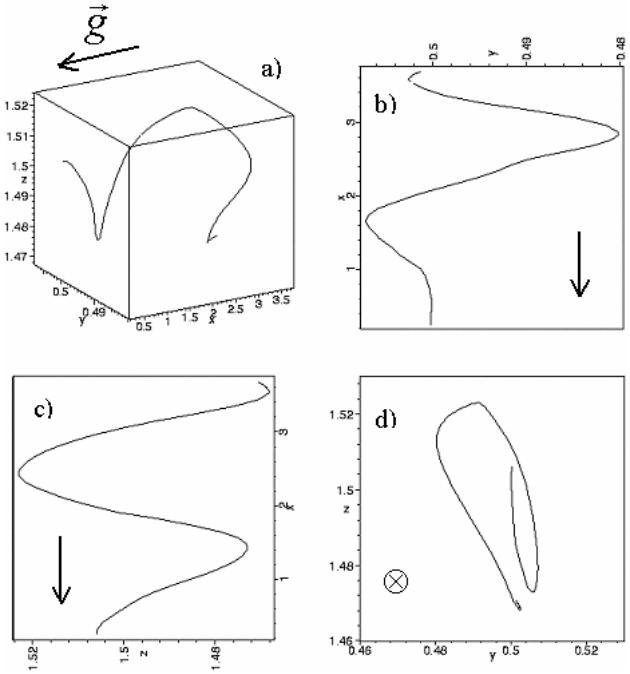

Fig 5. Trajectory of the bubble's centre of mass: (a) Bird eyes view, (b) - (d) 2D projections.

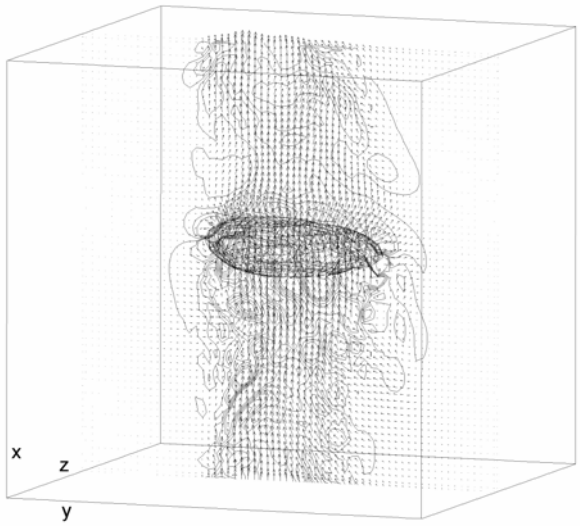

Fig 6. Visualisation of instantaneous bubble shape, velocity vectors, and vorticity contour lines in plane z = 0.5.

6. Conclusions

We have developed a computer code for the direct numerical simulation of certain aspects of bubble dynamics in a fluid by combining the Volume-of-Fluid method for tracking the gas-liquid interface with a new interface reconstruction algorithm. The code simulates well the underlying physical phenomena, as we have shown using typical 3D benchmark problems for single bubbles of different shape, wake, and motion. In particular, our code can be used to simulate even gas-liquid flow regimes at low Morton numbers and high bubble Reynolds numbers, where, as evidenced by many experiments, the bubble shapes and rising paths are irregular and non-steady, while the wake is turbulent. Such bubbles are of special practical relevance for general technical applications e.g. in power engineering and chemical engineering.

Although the simulations we presented in this paper were performed using a gas-liquid density ratio of 0.5, they showed that the Eötvös and Morton number are the most important similarity parameters that determine the bubble shape and the type of its wake. Since the bubble-induced turbulence is strongly associated with the flow around the bubble and the generation of vortices in its wake, it also follows that the Eötvös and Morton numbers will be important parameters in models for bubble-induced turbulence.

Our code is not restricted to density ratios of order 0.1 - 1. Future work is aimed at simulations in which the density ratio is varied but the Eötvös and Morton numbers are kept fixed. A qualitative verification of our code is also envisaged for bubble Reynolds numbers of about 400, where *regular* spiraling bubbles, undergoing *no* shape-oscillations, are expected according to detailed experimental investigations (Brücker, 1999). Longer-term research aims at investigating bubble-bubble and bubble turbulence interactions, by simulating the behavior of clusters of bubbles. The overall goal of this research is to contribute towards the development of improved statistical models to account for phenomena in engineering CFD codes for bubbly flows.

References

Ashgriz, N., Poo, J.Y., 1991. FLAIR: Flux line-segment model for advection and interface reconstruction. J. Comput. Physics 127, 449-468.

Bhaga, D., Weber, M.E., 1981. Bubbles in viscous liquids: shapes, wakes and velocities. J. Fluid Mech. 105, 61-85.

Brackbill, J.U., Kothe, D.B., Zemach, C., 1992. A Continuum Method for Modeling Surface Tension. J. Comput. Phys. 100, 335-354.

Brücker, C., 1999. Structure and dynamics of the wake of bubbles and its relevance for bubble interaction. Physics of Fluids 11, 1781-1796.

Clift, R., Grace, J.R., Weber, M.E., 1978. Bubbles, Drops, and Particles. Academic Press.

Fan, L.S., Tsuchiya, K., 1990. Bubble wake dynamics in liquids and liquid-solid suspensions. Butterworths-Heinemann Series in Chemical Engineering. Butterworths, Boston.

Grace J.R., 1973. Shapes and velocities of bubbles rising in infinite liquids. Trans. Instn. Chem. Eng. 51, 116-120.

Kothe, D.B., 1998. Perspective on Eulerian Finite Volume Methods for Incompressible Interfacial Flows. In: Free Surface Flows. H.C. Kuhlmann, H-J Rath, eds., Springer-Verlag, 267-331.

Sabisch, W., 2000. Dreidimensionale numerische Simulation der Dynamik von aufsteigenden Einzelblasen und Blasenschwärmen mit einer Volume-of-Fluid-Methode. Forschungszentrum Karlsruhe, Wissenschaftliche Berichte FZKA 6478, Juni 2000 (http://www.fzk.de/hbk/literatur/FZKA_Berichte/FZKA6478.pdf).

Sabisch, W., Wörner, M., Grötzbach, G., Cacuci, D.G., 1999. An improved volume of fluid method for numerical simulation of clusters of bubbles. In: M. Sommerfeld, ed., Proc.9th Workshop on Two-phase Flow Predictions, Merseburg, Germany, April 13-16, 1999, 175-184.

Scardovelli, R., Zaleski, S., 1999. Direct numerical simulation of free-surface and interfacial flows. Annu. Rev. Fluid Mech. 31, 567-603.

Schönauer, W., Häfner, H., Weiss, R., 1997. LINSOL, a parallel iterative linear solver package of generalized CG-type for sparse matrices. In: M. Heath et al., eds., Proc. 8th SIAM Conference on Parallel Processing for Scientific Computing (SIAM, Philadelphia, PA, 1997). CD-Rom (ISBN 0-89871-395-1).

Sethian, J.A., 1999. Level set methods and fast marching methods: evolving interfaces in computational geometry, fluid mechanics, computer vision, and materials science. 2nd edition. Cambridge University Press, Cambridge, UK.

Stewart, C.W., 1995. Bubble interaction in low-viscosity liquids. Int. J. Multiphase Flow 21, 1037-1046.

Tryggvason, G., Bunner, B., Ebrat, O., Tauber, W., 1998. Computations of multiphase flows by a finite difference/front tracking method. I. Multi-fluid flows. Von Karman Institute Lecture Notes, Von Karman Institute, Brussels, Belgium.

Wellek, R.M., Agrawal, A.K., Skelland, A.H.P., 1966. Shape of liquid drops moving in liquid media. AIChE Journal 12, 854-862.

Wörner, M., Sabisch, W., Grötzbach, G., Cacuci, D.G., 2001. Volume-averaged conservation equations for Volume-of-Fluid interface tracking. Proc. 4th Int. Conference on Multiphase Flow, ICMF-2001, New Orleans, Louisiana, U.S.A., May 27 - June 1, 2001.